Improved compound correction-electrical equivalent circuit modeling and double transform-unscented Kalman filtering for the high-accuracy closed-circuit voltage and state-of-charge co-estimation of whole-life-cycle lithium-ion batteries.

WANG, S., TAKYI-ANINAKWA, P., YU, C., JIN, S. and FERNANDEZ, C.

2022

Improved Compound Correction-Electrical Equivalent Circuit Modeling and Double Transform-Unscented Kalman Filtering for the High-Accuracy Closed-Circuit voltage and State-of-Charge Co-Estimation of Whole-Life-Cycle Lithium-Ion batteries

Shunli Wang, Paul Takyi-Aninakwa, Chunmei Yu, Siyu Jin, and Carlos Fernandez*

For complex energy storage conditions, it is necessary to monitor the state-of-charge (SOC) and closed-circuit voltage (CCV) status accurately for the reliable power supply application of lithium-ion batteries. Herein, an improved compound correction-electrical equivalent circuit modeling (CC-EECM) method is proposed by considering the influencing effects of ambient temperature and charge–discharge current rate variations to estimate the CCV. Then, an improved adaptive double transform-unscented Kalman filtering (ADT-UKF) method is constructed with recursive sampling data correction to estimate the nonlinear SOC. A dynamic window function filtering strategy is constructed to obtain the new sigma point set for the online weighting coefficient correction. For a temperature range of 5–45 °C, the CCV for the improved CC-EECM responds well with a maximum error of 0.008608 V, and the maximum SOC estimation error is 6.317%. The proposed ADT-UKF method improves the CCV and SOC estimation reliability and adaptability to the time-varying current rate, temperature, and aging factors.

1. Introduction

As an essential energy storage system, lithium-ion batteries are widely used in large-scale energy storage conditions with low self-discharge and high energy density advantages. For various electrical appliances, lithium-ion batteries are characterized by battery models effectively, such as electrochemical, neural network, composite and equivalent circuit modeling (ECM) methods, central difference transform, and real-time optimal forgetting factor correction strategies.[1–3] With the increasing application scope, the Gaussian process regression, data-driven, and Coulomb counting strategies are introduced.[4–7] In terms of temperature, the application conditions are complex and vary. Considering the discharge conditions of different state-of-charge (SOC) levels, the *k*-nearest neighbor regression is conducted with differential optimization strategies.[8–10] The lattice stability of battery cells is weakened gradually by the high-temperature influencing effect.[11] Meanwhile, it is affected by low-temperature conditions, which cause the lithium-ion exchange to slow down and pose a safety hazard due to the decrease in charge transfer.

The electrochemical–thermal coupling model is constructed to effectively improve the intermittent high-speed heating performance and reduce the influencing effect of temperature on the overall recyclable lithium-ion concentration of active particles. The nonlinear battery capacity degradation trend is obtained based on indirect health feature (IHF) and improved Gaussian process regression (GPR) modeling, combined with the changing trend analysis of current, voltage, and temperature.[12–15] Based on the data-driven method, a multi-stress low-temperature charging aging model is constructed, which is trained using the electrothermal measurement data without considering the internal battery mechanism, effectively simulating the battery response characteristics.[16–20] The construction of electrochemical impedance spectroscopy (EIS) simulates the electrochemical process inside the battery precisely, but it has defects such as complex structure and difficult parameter identification.[21]

S. Wang, P. Takyi-Aninakwa, C. Yu
School of Information Engineering
Southwest University of Science and Technology
Mianyang 621010, China
E-mail: wangshunli@swust.edu.cn

S. Wang
College of Electrical Engineering
Sichuan University
Chengdu 610207, China

S. Jin
Department of Energy Technology
Aalborg University
9220 Aalborg East, Denmark

C. Fernandez
School of Pharmacy and Life Sciences
Robert Gordon University
Aberdeen AB10-7GJ, UK

The aforementioned studies on electrochemical sensitivity analysis and electrochemical–thermal coupling can fully characterize the thermal performance of the charge–discharge process, providing a basis for the battery performance evaluation at low temperatures.

The lithium-ion battery requires special handling to avoid performance deterioration that results in severe damage or explosions. The scaling approach is realized for improved SOC estimation as one of the most significant factors for performance optimization.[22–25] The SOC estimation is conducted with non-electrical parameters and the uniform fiber Bragg grating (FBG). The estimation methods are used to determine the critical battery state and polynomial augmented model construction, including the immune genetic extended Kalman filtering, particle filtering, low-frequency EIS, double adaptive extended Kalman filter, adaptive H-infinity filter, and adaptive correction-unscented Kalman filter.[26–30]

The battery pack does not only deliver energy to the driving train for operation but also provides the required power under different conditions, so the SOC estimation is needed to make decisions on the operation accordingly.[8] The battery characteristics are modeled to monitor the SOC with several methods. The applied methods for the battery state estimation include the gray wolf particle filter, high-fidelity unscented particle filter, deep recurrent kernel, variable forgetting factor adaptive Kalman filter, adaptive Lyapunov super twisting observer, and machine learning.[31–33] The high-accuracy monitoring is conducted for the available energy and SOC estimation, including the data-driven nonparametric model, coupled electrochemical–thermal, and external measurable parameter coupling models.[34–36] The nonlinear curve fitting relationship is described using the simplification strategy for the thermal and nonlinear modeling processes.

In terms of data processing, the point-to-point calculation is adopted to obtain the curve fitting, where the battery characteristics are described effectively by the fractional variable-order model.[37–39] Combined with the experimental methods, the characteristic examination is conducted by the mathematical model based on real-time ECM.[40] The battery parameters are transformed into iterative calculations dynamically. The partial incremental capacity analysis is conducted with support vector regression and second-order extended Kalman filtering strategies.[41–44] The temperature and charge–discharge current rates are used as the main variables, in which the characteristics are initialized as dependent variables.

Accurate ECMs are constructed, and the expression of the mathematical relationship is established by considering the dual effect. Due to the effect of complex working condition changes, the measured external signals are mixed with noise information. Consequently, predictive models of battery degradation are conducted, and real-time sensitivity-based predictive control is constructed with the comprehensive single-particle-degradation model.[45–48] Its application prospects have attracted attention, and state estimation has become one of the main topics, which is transformed into the problem of obtaining implicit variables for the nonlinear time-varying battery system. The model parameters are nonlinear quantities and cannot be mea- sured directly.[49–51] The main factors and the variation effect are introduced into the ECM to build a suitable observer. The internal resistance is combined with OCV and current variation to simulate the instantaneous power output capacity within a certain period.

High-precision SOC estimation has an obvious influence on battery performance optimization. In this article, an improved compound correction-electrical equivalent circuit modeling (CC-EECM) strategy is constructed to characterize the nonlinear behavior of lithium-ion batteries by considering the modeling accuracy and complexity of the electrochemical properties. The mathematical relationship is established between the calculation accuracy and robustness so that the voltage variation effect is introduced into the error coefficient correction. Then, an adaptive double transform-unscented Kalman filtering (ADT-UKF) method is proposed with recursive sampling data correction as well as weighting coefficient optimization.

The remaining sections of this article are organized as follows: Section 2 introduces the mathematical analysis and model building process, including both the CC-EECM and ADT-UKF strategies; Section 3 describes the experimental analysis, in which the experimental test platform is described based on how the verification of the model is conducted effectively with the temperature and current rate variation effects and state estimation; Section 4 is the conclusion of the article.

2. Mathematical Analysis

2.1. Composite Modeling and Carrier Transport Collaborative Optimization

For the reliable energy supply–demand adaptive to low-temperature conditions, the composite modeling is carried out with the collaborative carrier transport optimization. It is used to solve battery performance optimization problems under complex working conditions such as time-varying temperature, diverse current magnification, working mode switching, and sudden output power change. The mathematical modeling, simulation, and multiparameter estimation of carrier states are combined to carry out the multidimensional coupling and collaborative simulation. The influence mechanism of low temperature is introduced to clarify the electrochemical electrothermal circuit composite model. The adaptive online parameter identification is conducted to adopt the piecewise optimization strategy and jointly improve the carrier transport process, realizing the composite modeling, rapid performance evaluation, and feedback adjustment of the carrier transport cooperative optimization. The overall research scheme is designed, as shown in Figure 1.

In Figure 1, based on the mechanism analysis and dynamic description of the internal chemical reaction, the collaborative optimization strategies of composite modeling, rapid performance evaluation, and carrier transport are explored to meet the safe and reliable energy supply needs of low-temperature lithium-ion batteries. Adopting a combination of internal working mechanism analysis, compound modeling, state evaluation method design, and collaborative optimization strategy improvement is conducted to reveal the carrier transport mechanism of the battery. Through multi-feature composite modeling, multi-scale performance evaluation, and multidimensional

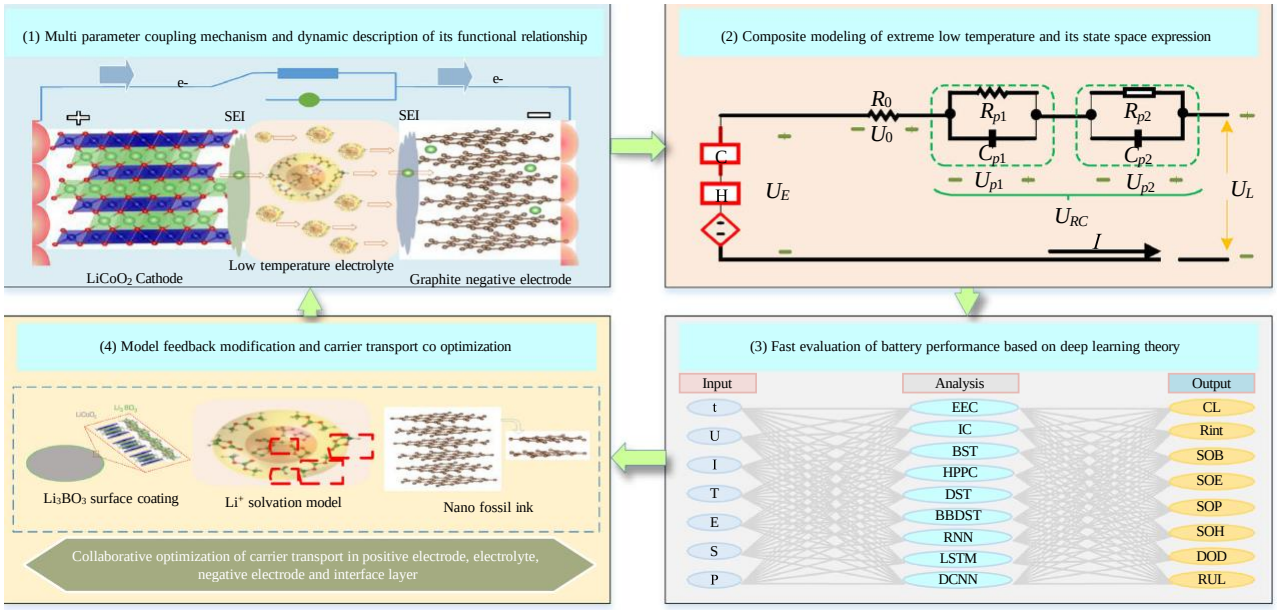

Figure 1. Composite modeling and carrier transport co-optimization for low-temperature lithium-ion batteries.

collaborative optimization, the requirements for a safe and reliable energy supply of lithium-ion batteries are met in low-temperature applications.

Based on the whole-life-cycle experimental data with a wide temperature range and the rapid evaluation results of battery performance under dynamic conditions, the output characteristics are analyzed to realize the mathematical description of working characteristics combined with environmental factors. Then, the cooperative carrier transport optimization is conducted, and the battery performance is evaluated using the test platform. The low-temperature battery performance is optimized by spiral iteration for the key links in the research scheme, including coupling mechanism analysis, composite equivalent simulation, rapid performance evaluation, and carrier transport collaborative optimization.

2.2. Compound Correction-Electrical Equivalent Circuit Modeling

Variables in the battery working process are closely monitored by the ECM mathematically. The cross-correlation parameters are extracted with a small iterative calculation number. Then, the time-varying variables for the temperature and current rate variations are obtained by the state-space description. The CC-EECM is constructed to mathematically describe the internal resistance and other time-varying variables necessary to evaluate the dynamic characteristics in terms of temperature changes and polarization effects due to the gradual variations of the OCV and temperature to minimize other influencing conditions. A large capacitor is added to the circuit modeling process to simulate the battery capacity and temperature effects. The schematic diagram of the improved CC-EECM is constructed, as shown in Figure 2.

In Figure 2, the proposed CC-EECM introduces two series-connected resistor–capacitor (RC) circuits. U_L is the CCV factor of the battery. The loop current is described by I_L. The current flow direction is positive during discharge and negative during charge. R_s is the self-discharge resistance. U_{OC} is the OCV factor, and R_0 is the ohmic resistance. C_b is the OCV influencing capacitor. E is the internal electromotive force. R_{p1} and C_{p1} are electrochemical RC components, respectively, for the mechanical

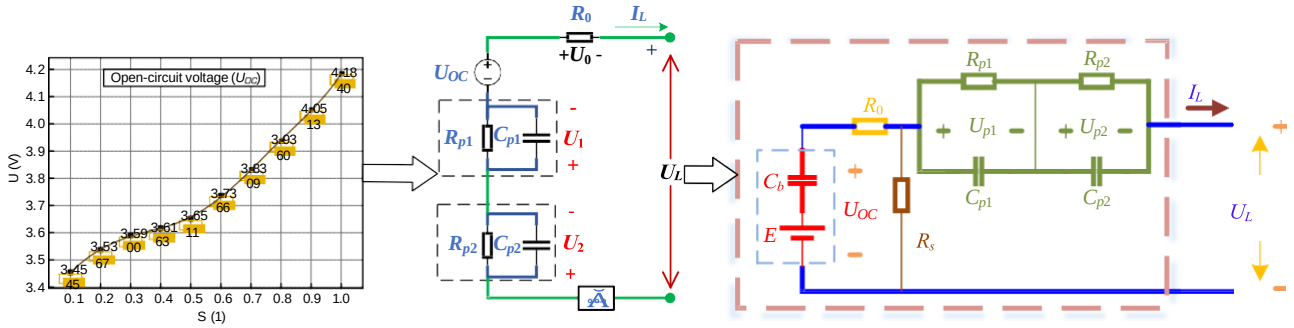

Figure 2. Schematic diagram of the improved compound correction-electrical equivalent circuit modeling (CC-EECM).

side-effects of isolating barriers. R_{p2} and C_{p2} are the concentration polarization RC components.

The proposed CC-EECM considers the changes in the various characteristic parameters. The battery factors consider the EEC modeling process as a function of temperature and SOC. Then, the modeling accuracy is further improved to simulate the ohmic polarization, electrochemical polarization, concentration polarization, and self-discharge characteristics. For the identification, the curve fitting method takes the data points into a function corresponding to different SOC levels and temperature conditions. A functional relationship between temperature and model parameters is established using the experimental data to minimize the complexity. After full consideration, improvements are made to the CC-EECM, considering the time-varying current rate, temperature, and aging characteristics of lithiumion batteries.

The mathematical relationship of U_{OC} and SOC is initialed as . After fitting every specific data onto the OCV values. The U_{OC} and S in the CC-EECM conducts the second-order unscented transform. Three constants of K_1, K_2, and K_3 fit the data effectively through different test comparisons. The mathematical state-space expression of the structural circuit model is obtained, as shown in Equation (1).

In Equation (1), k is the discrete-time point; U_{oc} is the CCV component; R_0 is the ohmic resistance; ocv is the flow current; U_{pC} is the polarization voltage; R_p is the polarization resistance; C_p is the polarization capacitance. R_p and C_p circuit reflects the polarization generation, as shown in Equation (2).

In Equation (2), U_{pC} is used as the polarization voltage. T is the sampling time. Substituting Equation (2) into Equation (1), the calculation process of UpO is obtained, as shown in Equation (3).

In Equation (3), the calculation process of U_{pC} is substituted into Equation (1) to obtain the calculation expression of U_{OC}. U_{OC} is then replaced by the state-space equation which forms a simplified discrete form, as shown in Equation (4).

In Equation (4), U_{LC} is the closed-circuit voltage at time point k. SC is the SOC value at time point k. I_{LP} is the current at time. point k. The coefficients of the iterative calculation procedure are a_1, a_2, ..., and a_6. Then, the parameter values are calculated by the least-square identification method, as shown in Equation (5).

In Equation (5), R_p is the polarization resistance; C_p is the polarization. Considering the convenience of project realization, T is initialized as 1 s. Also, the speed and efficiency of computing in the embedded system, as well as the occupation of storage space, are considered synchronously. Then, the parameters are calculated as shown in Equation (6).

In Equation (6), R_{cd} is obtained using the coefficients that are calculated using a_1, a_2, …, and a_6. The discrete form of the model is shown in Equation (7).

In Equation (7), S_{k-1} and S_k are the SOC values corresponding to the time point of k − 1 and k. U_{1k-1} and U_{1k} are the voltage values of the first-order RC circuit corresponding to the time point of k − 1 and k. S_{k-1} and S_k are the SOC values. U_{2k-1} and U_{2k} are the voltage values of the second order RC circuit. η is the Coulomb efficiency. Δt is the sampling interval. C is the rated capacity. i_k is the current at time point k. U_{OCk} is the corresponding OCV value. w_k is the process noise at time point k. The values of all contributing variables are obtained as shown in Equation (8).

In Equation (8), the state-space coefficient is Φ_{k-1}, and the control coefficient is Γ_{k-1}. The observed CCV value is calculated according to the second part of Equation (8) by taking U_{1k}, U_{2k}, I_k, and U_{OCk} into consideration. Their mathematical expression is shown in Equation (9).

In Equation (9), the state vector X_k is formed by the parameters of S_k, $U_{p1,k}$, and $U_{p2,k}$. The covariance of the system noise is Q. W_k is the observation noise with the covariance of R. The parameters that relate to SOC and terminal voltage are characterized by two RC series circuit components at the sampling time point k, respectively.

By carrying out the external characteristic analysis, the input and output characteristics are considered under different conditions based on the randomness and dynamic characteristics of the energy supply. The variation laws of core parameters are obtained accordingly, including open-circuit voltage (OCV), closed-circuit voltage (CCV), current magnification, SOC, aging degree, internal resistance, and temperature. Using the CC-EECM, the main influencing factors and logical relationships of output performance are explored. The static and dynamic response functions are established accordingly. The feature extraction and behavior description of input and output data are conducted at low temperatures under different working conditions, as shown in Figure 3.

In Figure 3, the improved CC-EECM is proposed to simulate the carrier transport process. Combined with the relationship analysis of the aging effect, performance attenuation, and characteristic parameters, the mathematical expression between internal parameters and influencing factors of battery performance is carried out. The charge transfer of lithium ions through the positive electrode/electrolyte interface, the solvation process of lithium ions entering the electrolyte, and the liquid phase migration of solvated clusters.

The lithium-ion de-solvation at the negative electrode–electrolyte interface is characterized by the charge transfer resistance R_{p1} and electric double-layer capacitance C_{p1}. The solid-phase diffusion inside the positive material lattice and the lithium-ion solid-phase diffusion through the negative SEI layer and the negative material layers are modeled and characterized as diffusion resistance R_{p2} and diffusion capacitance C_{p2}. These factors are used to further describe the input and output behavior characteristics accurately under low temperatures and complex current variation conditions. The influencing noise of complex working conditions is introduced to improve the modeling accuracy. It is used to describe the functional relationship between these model parameters and realize the state-space description. The mathematical description of the working characteristics is obtained and established with dynamic adaptability considering the capacity decline and temperature influence.

2.3. Influence Correction of the Ambient Temperature and Current Magnification

Fully considering the influence of hysteresis voltage and temperature on lithium-ion batteries, the hysteresis voltage is set as the corresponding characteristic description parameter combined with dynamic hysteresis analysis. Then, an iterative correction mechanism is established by integrating the temperature influence. The correction function is constructed based on the ambient temperature and current ratio variations. Considering the linear relationship between model parameters and current magnification, the framework of the model parameter correction function is established with its approximate nonlinear relationship with temperature. Furthermore, the online full parameter identification is designed with real-time feedback correction to analyze and correct the influence of working condition noise. Then, the multi-timescale effective characterization of model parameters is realized, as shown in Figure 4.

In Figure 4, the effective working condition influence is considered, and the measurement error is partially separated to correct the components of the input interface. Then, the error correction effect is evaluated to optimize the observation parameters of the composite CC-ECCM. Finally, the decoupling

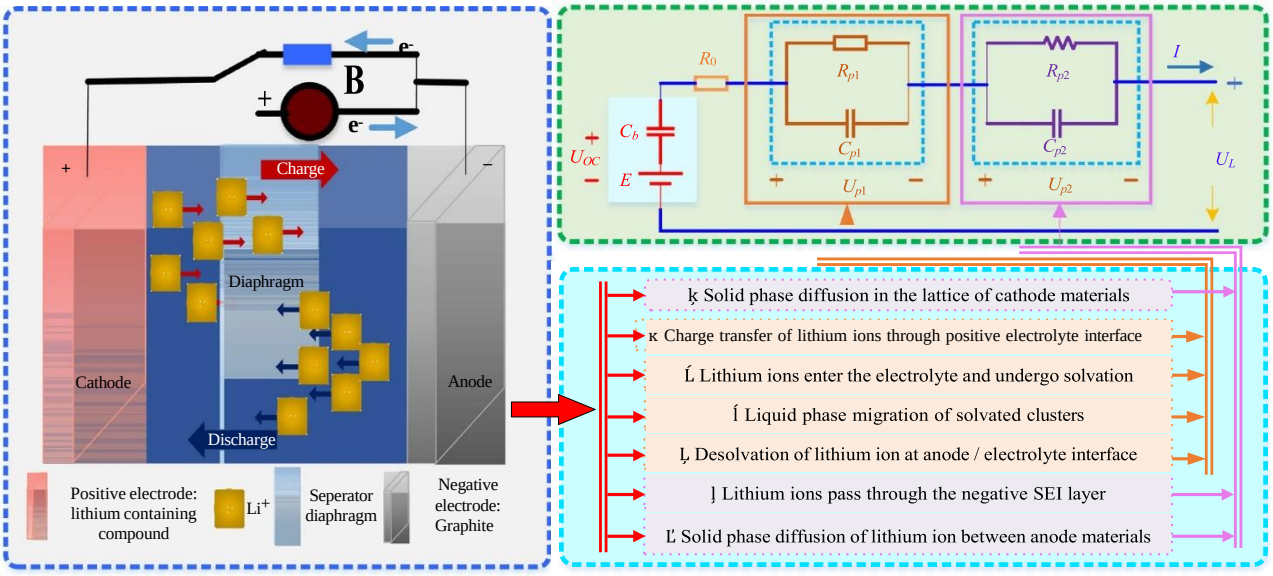

Figure 3. Feature extraction and behavior description at low temperatures under different conditions.

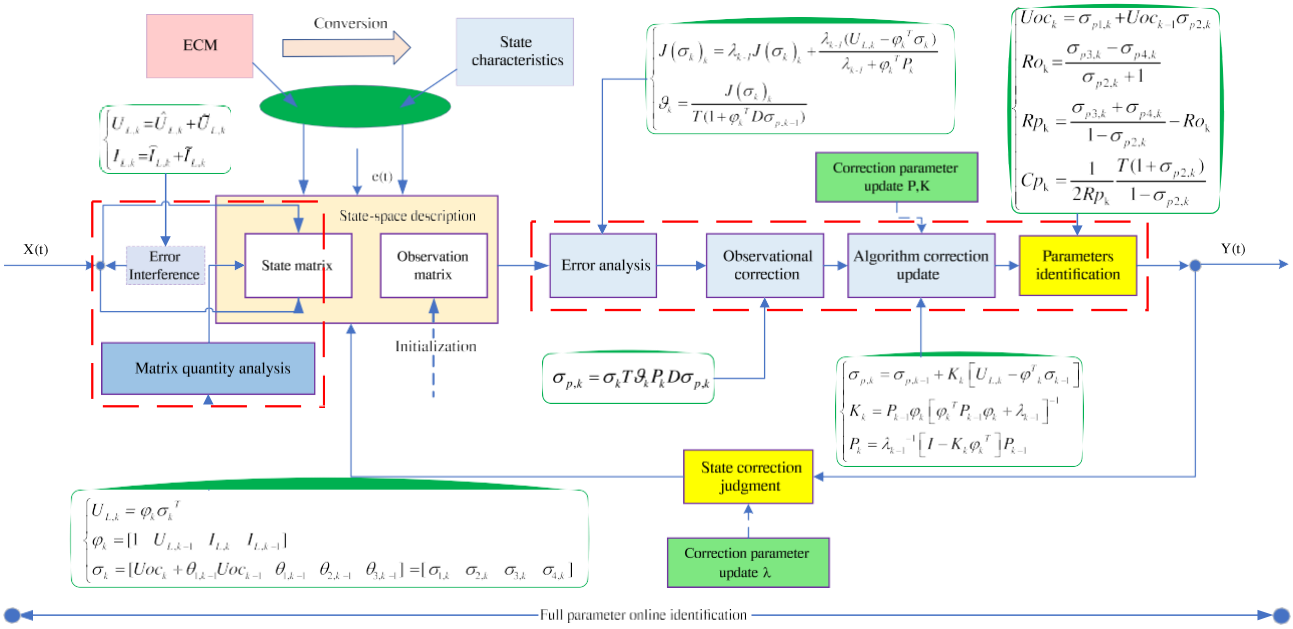

Figure 4. Structural design and optimization of characteristic multi-timescale model.

analysis of the model parameters is completed, and the online full parameter identification is realized. The external characteristics of the battery parameters are considered, including voltage, current, and temperature variation. The voltage separation error is corrected to track the model parameter representation of the internal characteristics. Consequently, a reliable characterization mechanism for the overall performance is obtained. The real-time calibration is carried out based on the correction of temperature and current magnification. The feedback correction structure of the identification process is constructed to realize the online identification of all model parameters. Taking CCV closely as the output parameters that are related to the observation equation, the influence of charge–discharge current ratio and temperature variation is evaluated. The state-space description method and correction mechanism are optimized by weighting both the accuracy and complexity of the calculation process.

2.4. Improved Adaptive Double Transform-Unscented Kalman Filter

To ensure the co-estimation accuracy of CCV and SOC, the mathematical state-space description of the CC-EECM is introduced into the improved ADT-UKF method with an iterative calculation. It is constructed in the iterative calculation process for the comparative error analysis. The state-space description is obtained as shown in Equation (10).

In Equation (10), soc is the state transition model. SOC is the nonlinear control-input model. X_k is the true state variable, and Y_k is the measurement equation. U_k is the controlinput vector. Consequently, the specific process is obtained and the initial value of the model parameters is calculated as shown in Equation (11).

In Equation (11), the unscented transform is conducted twice to minimize error and correct initial state divergence. Therefore, the improved ADT-UKF method has a dual unscented transform handled accordingly as shown in Equation (12).

In Equation (12), the initial parameter values are obtained through the convolution operation. The point data set divergence is calculated from the estimated state value. The weighting coefficient ω_{mi} and the sigma point estimation values are combined for the battery state estimation, as shown in Equation (13).

In Equation (13), the mathematical model and the dual unscented transform of the new sigma points are obtained and corrected. Consequently, the sigma data point set is introduced into the observation equation. The measurement equation is established as shown in Equation (14). In Equation (14), the autocorrelation and cross-correlation coefficients are calculated accordingly as shown in Equation (15). In Equation (15), the calculation process is different from the traditional UKF method because the proposed ADT-UKF method introduces the weighting correction of the battery characteristics, as shown in Equation (16). In Equation (16), the iterative structural calculation is established.

When applied to the wide-temperature-range conditions, the whole-life-cycle state estimation is a major challenge, so the resolution of these contradictions determines the vitality and SOC estimation. Furthermore, the influence of internal balance current is also considered for high-precision state monitoring, in which the estimation procedure is designed to make the model suitable for practical application. Also, the synthesized diagnosis is investigated to realize its safety protection. The dynamic propagation characteristics are introduced into the multiple time-variant input–output channels. The quantitative model verification is conducted for the effective battery performance characteristics, thereby realizing the wide-temperature-range electrothermal modeling and online state estimation. The identification diagnosis is applied to the energy storage systems, which is implemented by accurate mathematical modeling through incremental capacity analysis combined with gray correlation.

2.5. Composite characterization of the Low-Temperature Aging Process

Combined with the full parameter online identification, the multidimensional constraints are described. The correction coefficient of temperature and capacity is added to further optimize the effect of model parameter identification, forming a key parameter identification and calibration mechanism combined with temperature correction. The variation law of the key parameters is extracted by considering different current magnifications and temperature influences. Then, the obtained parameters are substituted into the constructed composite model. The online identification and effect verification process of model parameters is designed under multiple constraints. Consequently, multiple parameter identification and an iterative calculation framework are formed, as shown in Figure 5.

In Figure 5, multi-feature model parameters and online temperature-capacity correction are at the core of the estimation method. Combined with the real-time acquisition of SOC value, it can provide a reliable correction basis for observation and measurement.

The time scale preset can effectively provide limited analysis under duration. The discharge capacity is measured in the low-temperature aging process to conduct the varying discharge ratio and temperature analysis. The performance test is realized under mixed pulse discharge current rates, and the

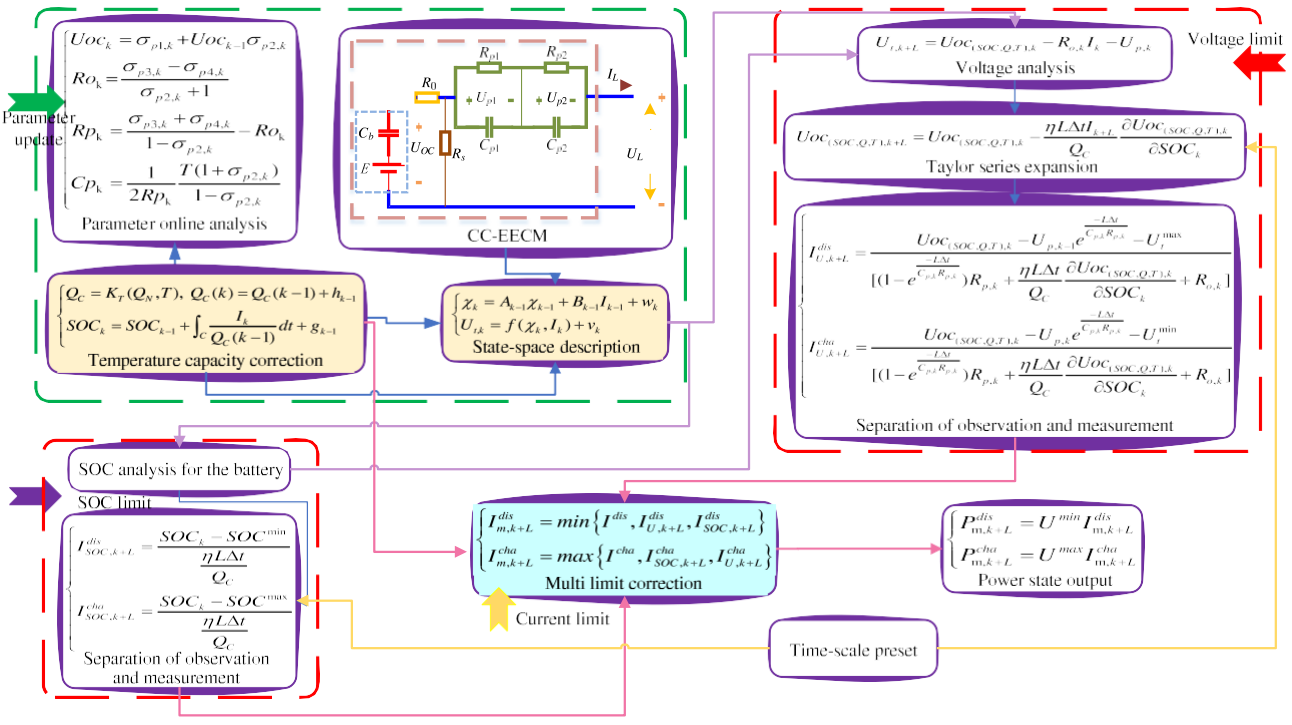

Figure 5. The multi-feature model parameter identification and iterative calculation framework.

variation law of model parameters is obtained with its dynamic description.

3. Experimental Verification

3.1. Testing Platform Design and Implementation

The lithium cobalt oxide (HTCNR18650-2200 mAh-3.6 V) battery is used for the experimental tests. Specific experimental procedures are designed for capacity determination, hybrid power pulse characterization (HPPC), OCV-SOC measurement, and Beijing bus dynamic stress test (BBDST). The constructed platform used for the tests in this study is shown in Figure 6.

The battery OCV test procedure is designed as follows: 1) Full charge with CC–CV mode is conducted. After 5 h of rest, the OCV measurement is conducted when the SOC value equals 100%; 2) The rated capacity is discharged by 5% or the minimum cut-off voltage. Then, the OCV value is recorded after the batter- ies are shelved for 5 h. The whole cycle test procedure is designed, as shown in Figure 7.

In Figure 7, the CC–CV charge procedure is used. Then, it is discharged to the minimum cut-off voltage at the 0.3C current rate of the CC mode. This step is repeated for three cycles, which are also performed in the time-varying situation. In the HPPC test procedure, continuous charge-discharge treatment is applied to the dynamic time-varying SOC levels. First, the CC–CV charge is realized at 0.3C, and the battery is shelved after it attains maximum terminal voltage; 2) Shelving for 5 h is conducted before the next test profile; 3) The CC discharge pulse of 1C is applied for 5 min followed by 1 h of rest. CC mode is used to ensure that

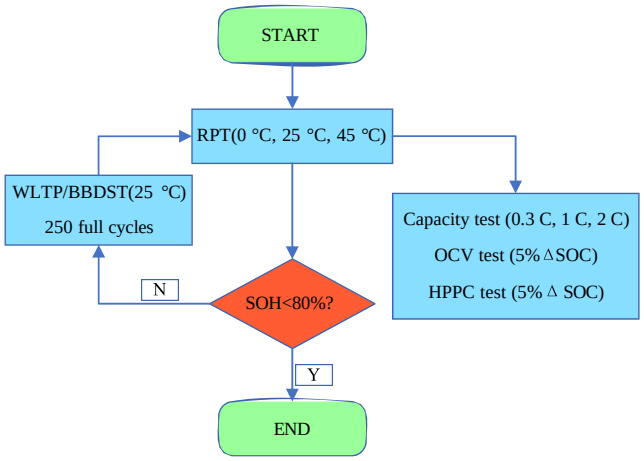

Figure 7. The whole structure of the experimental test.

the SOC variation is 5%. Then, the working characteristics are obtained for the SOC levels of 100%, 95%,..., and 5%. The testing operation in step 3) is repeated until the minimum voltage of 3.00 V is reached.

For the complex BBDST and characteristic determination, a testing procedure is designed in which the HPPC, OCV, and temperature variation for the process are under investigation. The procedure for the HPPC and OCV tests is designed and conducted as well as BBDST. The variation of every single battery is obtained by the calculation from the battery packs, as shown in Equation (17).

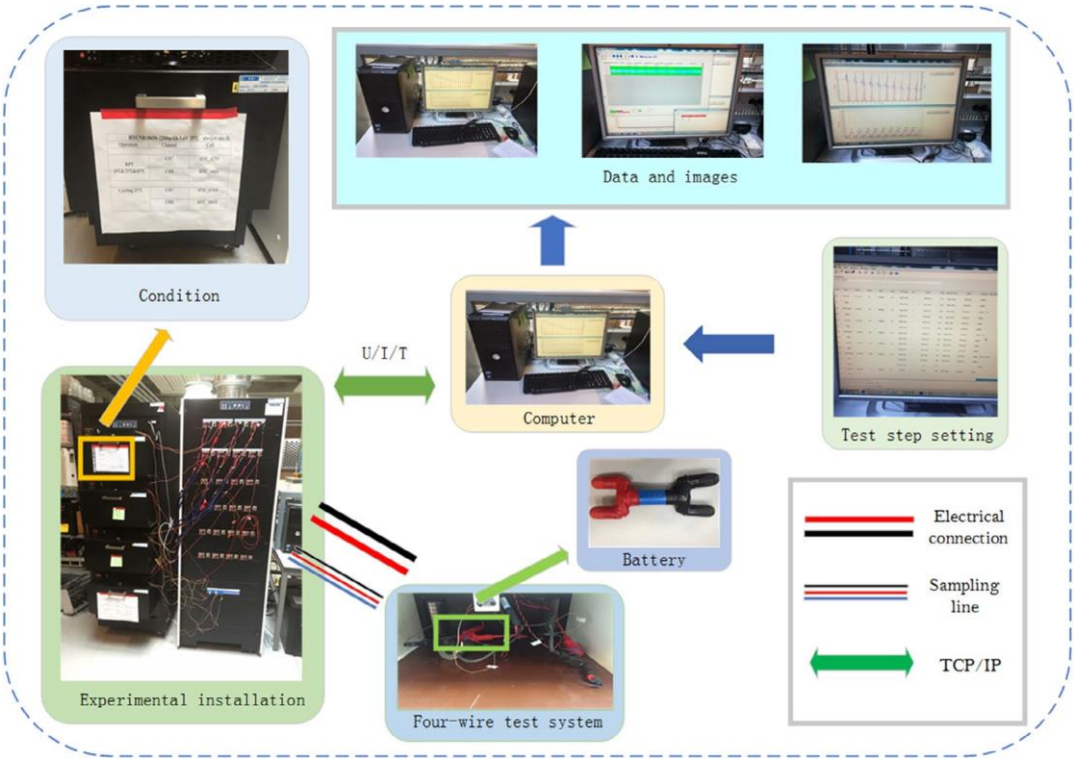

Figure 6. Experimental platform for complex condition tests.

$$P_c = \frac{U_c Q_c}{U_c Q_c} P_b = \lambda_b P_b \quad (17)$$

In Equation (17), λ_b is the equivalent coefficient, b is defined as the battery pack, and c is the single battery cell. The testing power is enlarged during the BBDST experiment to test for the overload capacity, as shown in Equation (18).

$$P_c^0 = \alpha P_c \quad (18)$$

In Equation (18), α is the coefficient. The total normal pack voltage of an EV is 384 V with a capacity of 360 Ah. The normal voltage of a single battery cell is 3.6 V with 2.2 Ah. Since $\alpha = 5$, the power for a single battery cell is calculated, as shown in Equation (19).

$$P_c^0 = \alpha \frac{U_c Q_c}{U_c Q_c} P_b = 5 \times \frac{3.6 \times 2.2}{384 \times 360} \times P_b = 2.8646 \times 10^{-4} \times P_b \quad (19)$$

In Equation (19), after charging with the CC–CV method, the current discharge pulse is applied according to the BBDST experiment until the minimum cut-off voltage of 3.00 V is reached to calculate the power value. With an average current rate of 1C, the current value is calculated using the equation $I = P/U$, in which $U = 3.60$ V. As every single step of the BBDST experiment is conducted for 300 s, the test lasts for 12 cycles until total discharge, which leads to the CC–CV charge. The BBDST procedure can be designed and implemented accordingly, as shown in Figure 8.

In Figure 8, the single BBDST is conducted with a total of 3.5 h of treatment. Considering a dataset, a 3-day test for the dataset is suitable, so the cycling number is set as $\frac{24 \times 3}{3.5} = 20.57$. A cycle number of 20.57 is impossible to set, so it is defined for each dataset as 20 for ease of application and calculation purposes.

3.2. Temperature and Current Rate Variation Effects

The time-varying temperature and current rate effects are conducted using the temperature test chamber and battery testing equipment. With a low-temperature effect, the energy and power decrease rapidly as the discharge depth increases. An irreversible aging process takes place, so the output performance variation of the battery is affected by the cyclic current charge–discharge pulses. Besides the irreversible variation of the electrode material, physical structure, and lithium-ion transfer rate, the electrolyte is organic, and its conductivity is reduced under low-temperature conditions. This reduction in conductivity causes a rapid increase in internal resistance, resulting in performance deterioration. The resistance increase feedback promotes a quick temperature rise, which adversely affects the battery characteristics and performance. A capacity test at a temperature of 5 °C is conducted by considering the current rate variation for effective experimental test results, as shown in Figure 9.

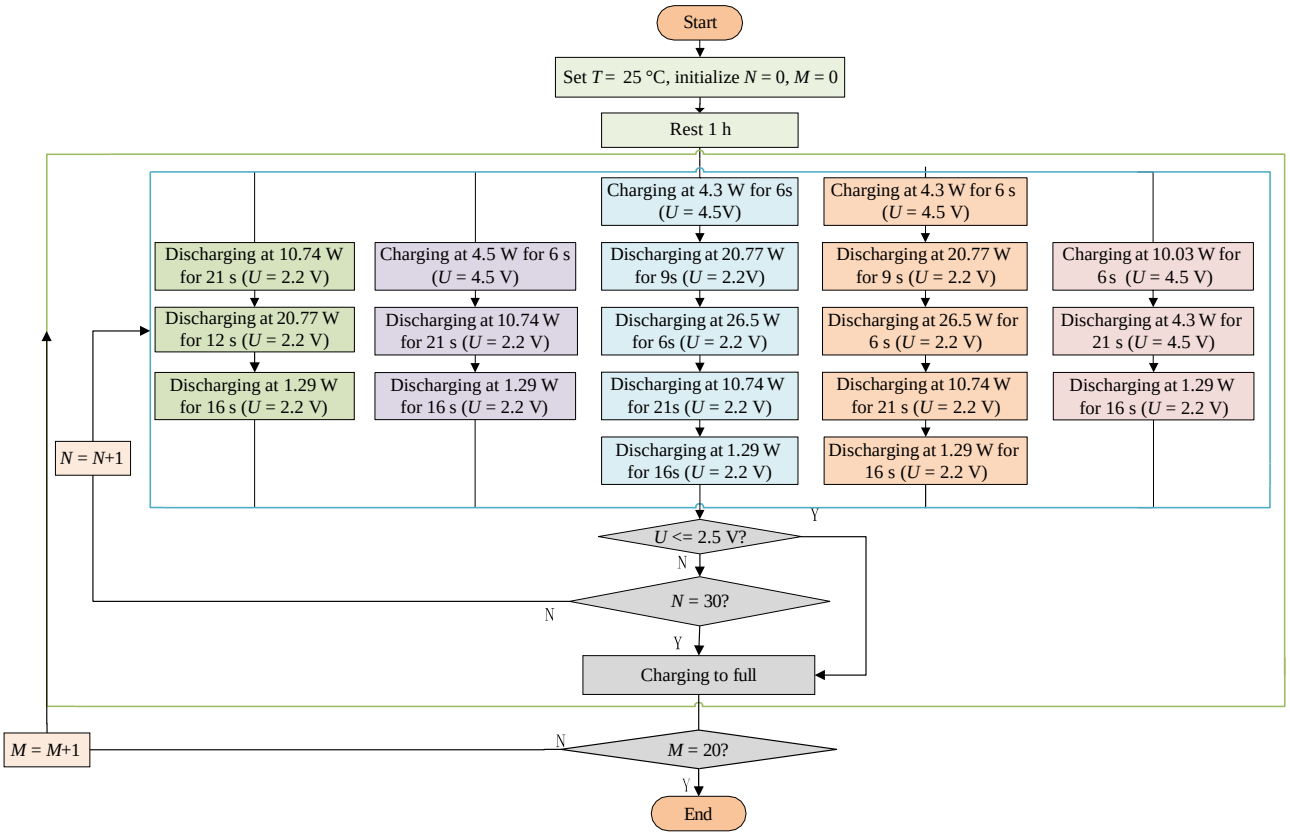

Figure 8. The experimental Beijing bus dynamic stress test (BBDST) procedure for the lithium-ion battery.

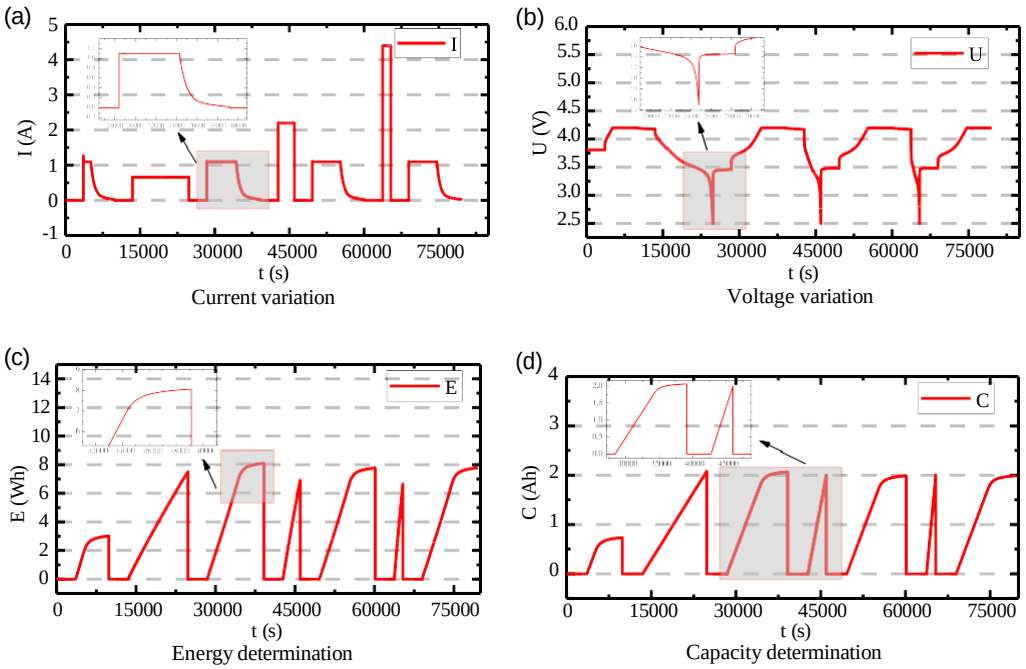

Figure 9. Capacity determination considering the current rate variation for 5 °C. a) Current variation, b) voltage variation, c) energy determination, and d) capacity determination.

In Figure 9, the nominal capacity is 2.079 Ah for 0.3C, 1.999 Ah for 1C, and 2.006 Ah for 2C. A time-varying test is also conducted at 45 °C conditions. The test results are shown in Figure 10.

In Figure 10, the rated capacity is 2.36 Ah for 0.3C, 2.34 Ah for 1C, and 2.325 Ah for 2C. Consequently, the battery's capacity decreases under high-temperature conditions. The significant factor changes are also analyzed to obtain a mutual effect and coupling relationship of battery parameters, including OCV, CCV, cell voltage, flowing current, resistance, and temperature. The characteristics are compared for various SOC levels, and the CCV variation towards temperature change is analyzed. The main parameter variation is compared to established logical and dynamic response functions. Then, the characteristics are obtained by the testing schedule design, including CC charge, varying current discharge, charge–discharge pulse-current, OCV-SOC, and temperature-capacity tests. The influencing

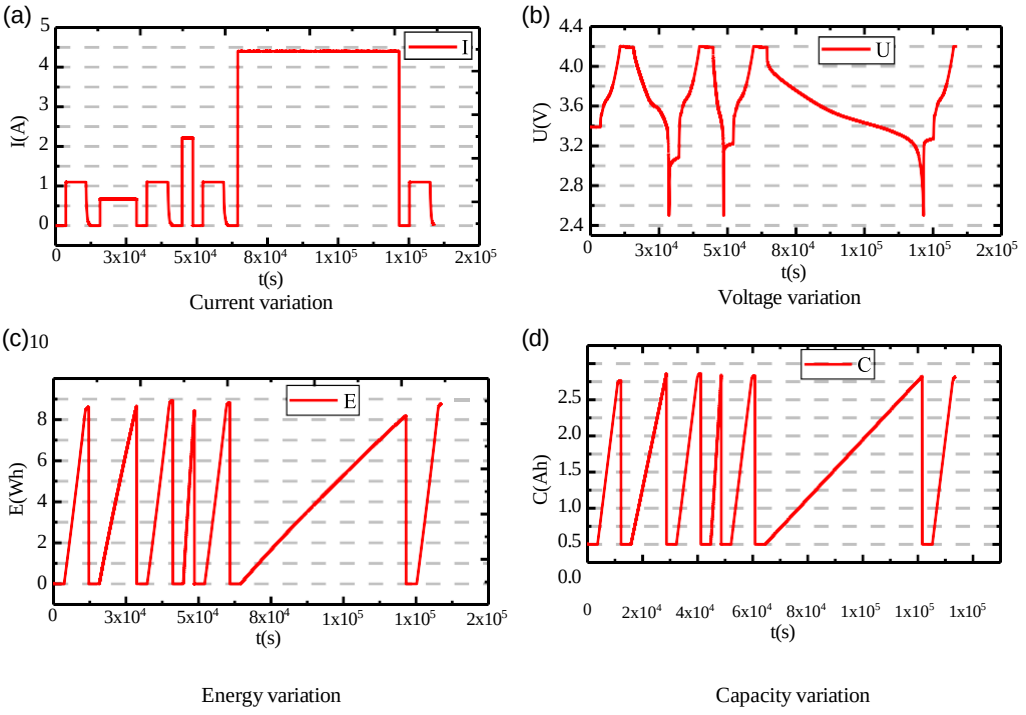

Figure 10. Capacity determination considering the current rate variation for 45 °C. a) Current variation, b) voltage variation, c) energy variation, and d) capacity variation.

effect analysis is conducted toward the CCV variation, and the characteristics are analyzed for time-varying ambient conditions. For the OCV and HPPC tests, the CCV is measured in real time. Meanwhile, the CCV value and CC-EECM parameters are obtained for various SOC levels. During the testing process, the battery is charged to full capacity until the CCV equals 4.20 V for 0.3C with 40 m of rest. The procedure is then turned into the following state levels for the cyclic BBDST. The test results are expressed with a functional relationship description. The single testing procedure is designed and realized: 1) Full capacity charge to get the SOC equal to 1; 2) 40 m of rest; 3) Discharge for 5% SOC; 4) 30 m of rest; 5) The cyclic charge–discharge sequence from 2) to 4) is repeated 11 times until the SOC reaches 0. The test results obtained are shown in Figure 11.

In Figure 11, the OCV value is measured toward the time-varying SOC levels to obtain time-varying model parameters. The improved ADT-UKF iterative estimation-correction method imposes the OCV-SOC function by introducing the polynomial and look-up table. The OCV-SOC functional relationship is also established for varying temperature conditions. The real-time CCV value is measured for iterative calculation using the improved ADT-UKF method with the modeling parameter determination. The functional relationship between OCV and SOC has a nonlinear positive functional relationship in which the OCV value decreases along with the SOC reduction, considering both the SOC and temperature variations.

Based on the experimental analysis, the OCV-SOC functional relationship is different, which is a core factor for the model-based SOC estimation. The higher the temperature, the lower the discharging minimum cut-off voltage, and the discharge capacity increases with the variation. The OCV-SOC varying relationship shows a downward tendency, so more power cannot be used effectively. Subsequently, in the low state interval, OCV-SOC functional relationship curves vary with the SOC changing process. By comparison, the OCV-SOC has a variable relationship for different temperature variations. The mathematical analysis of the CC-EECM is realized with real-time current rate variation. The current rates are significant in the CCV, OCV, capacity, internal resistance, and SOC estimations are conducted considering the temperature limitation. The temperature ranges from 5 to 45 °C. The available capacity reduces when the temperature increases, so the SOC value also varies for the same level of CCV.

3.3. Complex working condition estimation analysis

The mathematical voltage-correction functions are constructed by comparing the OCV-SOC relationship at time-varying temperature conditions. The experimental result shows that the expression of the mathematical characteristic is affected by the temperature variation to correct the predicted SOC value. The OCV-SOC variation is introduced into the SOC estimation process by considering the temperature variation effect, in which the modeling CC-EECM parameters under the ambient condition variation are substituted into the iterative calculation process. The proposed ADT-UKF method is first verified by a varying current discharge with an average rate of 3C with the combined iterative state-space equation. The combined time-varying discharging current rate test is designed under complex power supply working conditions. The CC-EECM parameters are introduced into the improved ADT-UKF estimation-correction process, and the current is changed for the complex working condition tests. The CCV traction and SOC estimation results are obtained, as shown in Figure 12.

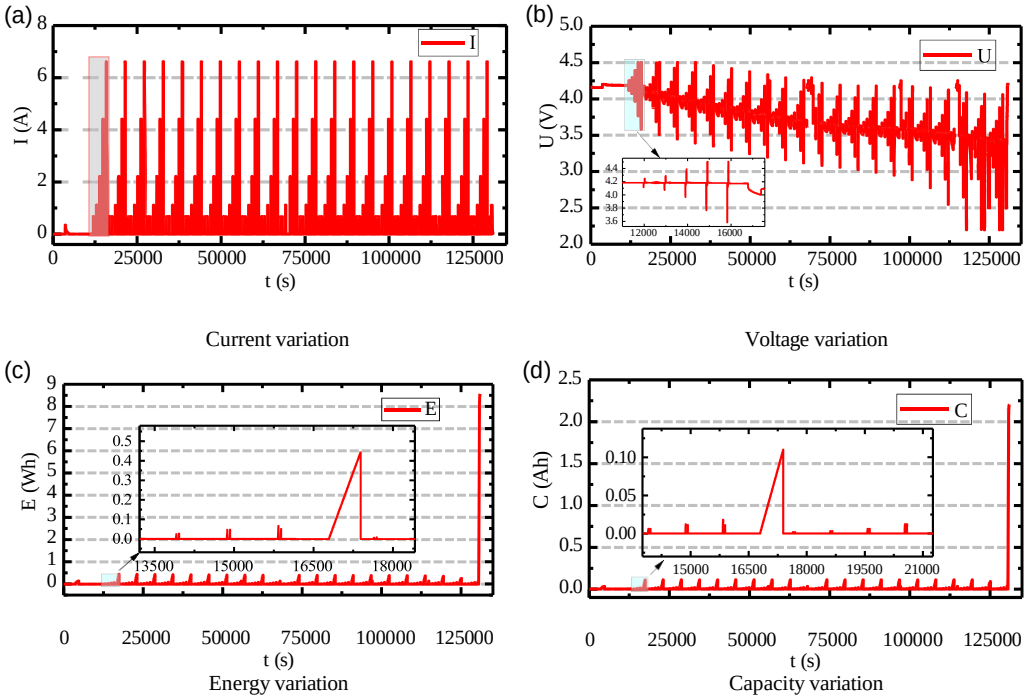

Figure 11. The open-circuit voltage (OCV) and hybrid power pulse characterization (HPPC) tests at 5 °C. a) Current variation, b) voltage variation, c) energy variation, and d) capacity variation.

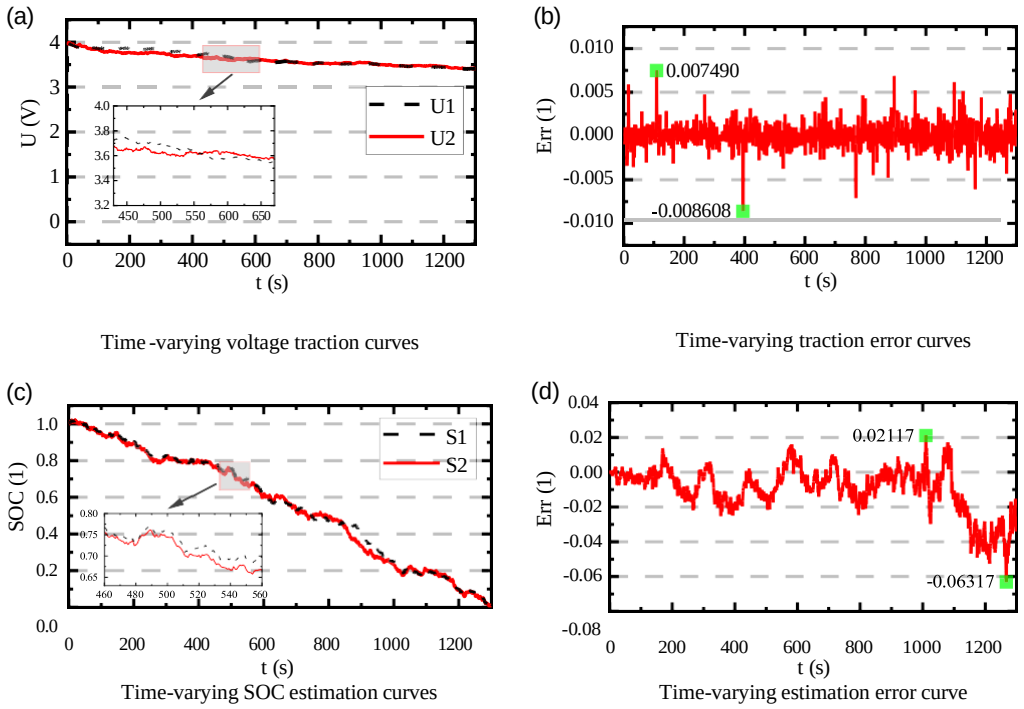

Figure 12. Closed-circuit voltage (CCV) traction and state-of-charge (SOC) estimation effect analysis. a) Varying current state estimation, b) varying current state estimation error, c) varying current-voltage traction, and d) varying current-voltage traction error.

In Figure 12, it can be observed that the CC-EECM tracks the CCV traction process for the whole traction process by taking advantage of particle re-sampling and continuous training, and the improved ADT-UKF method has an optimal experimen- tal effect on the SOC estimation. For the CCV traction, the maximum error observed is 0.008608 V, and the maximum SOC error estimated by the improved ADT-UKF method is 6.317%. The iterative estimation and correction are conducted for the adaptive high-precision SOC estimation. The estimation curve approaches the actual value effectively, revealing a high converging tendency. Also, the hierarchical SOC estimation is conducted considering the environmental and load-change effects and the aging performance with life decay.

4. Conclusion

An improved CC-EECM and ADT-UKF method are constructed to realize real-time CCV traction and SOC estimation, respectively. The more accurate and intricate the modeling of the electrochemical characteristics, the better the CC-EECM technique is at describing the nonlinear behavior of lithium-ion batteries. The calculation accuracy and resilience have a mathematical relationship established between them so that the voltage variation effect can be included in the error coefficient correction. The ADT-UKF method is then proposed along with recursive sampling data correction and optimization of the weighting coefficient. They have the advantages of high accuracy and long-term adaptivity, which also characterize the polarization and transient effects in the pulse-current charge–discharge process. The proposed CC-EECM and ADT-UKF methods reduce the nonlinear functional relationship effectively. At a temperature range of 5 to 45 °C, the output voltage responds well with a maximum error of 0.008608 V, and the maximum SOC estimation error is 6.317%. With high-accuracy CCV and SOC estimation results, the calculation complexity is moderate to avoid the diverge performance, reducing the linearization errors and providing useful references for BMS applications.

Acknowledgements

The work is supported by the National Natural Science Foundation of China (No. 62173281).

Conflict of Interest

The authors declare no conflict of interest.

Author Contributions

S.W.: Conceptualization, Methodology, Software; P.T.-A.: Software and validation; C.Y.: Visualization, Investigation; S.J.: Data curation, writing, and original draft preparation; C.F.: Writing-reviewing and editing.

Data Availability Statement

The data that support the findings of this study are available from the corresponding author upon reasonable request.

Keywords

adaptive double transform-unscented Kalman filter, closed-circuit voltage, compound correction-electrical equivalent circuit modeling, lithium-ion batteries, state-of-charge

Received: August 10, 2022
Revised: September 6, 2022

[1] Y. Zheng, Z. Shi, D. Guo, H. Dai, X. Han, *J. Power Sources* 2021, *489*, 229505.
[2] F. Lotfi, S. Ziapour, F. Faraji, H. D. Taghirad, *Int. J. Electr. Power Energy Syst.* 2020. *117*, 105666.
[3] A. Fotouhi, D. J. Auger, K. Propp, S. Longo, *IEEE Trans. Power Electron.*, 2018, *33*, 5847.
[4] K. Ando, T. Matsuda, D. Imamura, *J. Energy Chem.*, 2021, *53*, 285.
[5] Z. Liao, S. Zhang, K. Li, M. Zhao, Z. Qiu, D. Han, G. Zhang, T. G. Habetler, *J. Energy Storage* 2020, *27*, 101065.
[6] L. X. Wu, K. Liu, H. Pang, *Electrochim. Acta*, 2021. *368*, 137604.
[7] L. Wu, H. Pang, Y. Geng, X. Liu, J. Liu, K. Liu, *Int. J. Energy Res.* 2022, *46*, 11834.
[8] Y. Fang, Q. Zhang, H. Zhang, W. Xu, L. Wang, X. Shen, F. Yun, Y. Cui, L. Wang, X. Zhang, *IET Power Electron.* 2021, *14*, 1515.
[9] G. Dong, J. Wei, Z. Chen, *Int. J. Electr. Power Energy Syst.* 2018, *99*, 516.
[10] N. X. Yang, M. Wang, J. Wang, L. Wang, Y. Fu. *Energy Technol.* 2021. *9*, 2000924.
[11] J. Zhong, T. Wang, L. Wang, L. Peng, S. Fu, M. Zhang, J. Cao, X. Xu, J. Liang, H. Fei, X. Duan, B. Lu, Y. Wang, J. Zhu, X. Duan, *Nano-Micro Lett.* 2022, *14*, 50.
[12] L. Chen, H. Wang, B. Liu, Y. Wang, Y. Ding, H. Pan, *Energy* 2021, *215*, 119078.
[13] S. Zhu, J. Han, H.-Y. An, T.-S. Pan, Y.-M. Wei, W.-L. Song, H.-S. Chen, D. Fang, *J. Power Sources*, 2020, *456*, 227981.
[14] N. Michel, P. Wei, Z. Kong, A. K. Sinha, X. Lin, *eTransportation* 2022, *12*, 100173.
[15] I. Traskunov, A. Latz, *Energy Technol.* 2021, *9*, 2000861.
[16] C. Lee, S. Jo, D. Kwon, M. G. Pecht, *IEEE Trans. Ind. Electron.* 2021, *68*, 2659.
[17] E. Kwak, S. Jeong, J.-H. Kim, K.-Y. Oh, *J. Power Sources*, 2021, *483*, 229079.
[18] C. Vidal, O. Gross, R. Gu, P. Kollmeyer, A. Emadi, *IEEE Trans. Veh. Technol.* 2019, *68*, 4560.
[19] T. Wang, X. Wu, S. Xu, H. Hofmann, J. Du, J. Li, M. Ouyang, Z. Song, *J. Power Sources* 2018, *401*, 245.
[20] M. Luo, Y. Guo, J. Kang, L. She, Z. Geng, *Ionics* 2018, *24*, 1907.
[21] J.-Q. Li, L. Fang, W. Shi, X. Jin, *Energy* 2018, *148*, 247.
[22] J. Zhengxin, S. Qin, W. Yujiang, W. Hanlin, G. Bingzhao, H. Lin, *Energy* 2021. *230*, 120805.
[23] J. Kumberg, M. Baunach, J. C. Eser, A. Altvater, P. Scharfer, W. Schabel, *Energy Technol.* 2021, *9*, 2000889.
[24] D. Gong, Y. Gao, Y. Kou, *Energy Technol.* 2021, *9*, 2100235.
[25] J. Zhang, X. Liu, C. Chen, A. Simeone, *Energy Technol.* 2020, *8*, 2000624.
[26] J. X. Chen, X. Feng, L. Jiang, Q. Zhu, *Energy* 2021, *227*, 120451.
[27] X. Lai, L. He, S. Wang, L. Zhou, Y. Zhang, T. Sun, Y. Zheng, *J. Cleaner Prod.* 2020, *255*, 120203.
[28] J. Sun, C. Tang, X. Li, T. Wang, T. Jiang, Y. Tang, S. Chen, S. Qiu, C. Zhu, *eTransportation* 2022, *11*, 100149.
[29] Q. Yang, J. Li, R. Yang, J. Zhu, X. Wang, H. He, *eTransportation* 2022, *11*, 100151.
[30] X. Feng, Y. Merla, C. Weng, M. Ouyang, X. He, B. Y. Liaw, S. Santhanagopalan, X. Li, P. Liu, L. Lu, X. Han, D. Ren, Y. Wang, R. Li, C. Jin, P. Huang, M. Yi, L. Wang, Y. Zhao, Y. Patel, G. Offer, *eTransportation* 2020, *3*, 100051.
[31] K. D. Rao, A. H. Chander, S. Ghosh, *IEEE Trans. Veh. Technol.* 2021, *70*, 3218.
[32] T. C. Ouyang, P. Xu, J. Chen, Z. Su, G. Huang, N. Chen, *Energy* 2021, *226*, 120348.
[33] W. Kim, P.-Y. Lee, J. Kim, K.-S. Kim, *IEEE Trans. Veh. Technol.* 2021, *70*, 5638.
[34] T. Zhang, N. Guo, X. Sun, J. Fan, N. Yang, J. Song, Y. Zou, *Sustainability* 2021, *13*, 5166.
[35] P. Ladpli, F. Kopsaftopoulos, F.-K. Chang, *J. Power Sources* 2018, *384*, 342.
[36] H. Pang, J. Jin, L. Wu, F. Zhang, K. Liu, *J. Electrochem. Soc.* 2021, *168*, 090552.
[37] H. F. Khan, A. Hanif, M. U. Ali, A. Zafar, *J. Energy Storage* 2021, *41*, 102843.
[38] C. Jiang, S. Wang, B. Wu, C. Fernandez, X. Xiong, J. Coffie-Ken, *Energy* 2021, *219*, 119603.
[39] L. Zhou, L. He, Y. Zheng, X. Lai, M. Ouyang, L. Lu, *J. Energy Storage* 2020, *28*, 101252.
[40] P. Wang, X. Lou, C. Li, X. Hu, Q. Yang, B. Hu, *Nano-Micro Lett.* 2018, *10*, 652.
[41] Z. Xia, J. A. Abu Qahouq, *IEEE Trans. Ind. Appl.* 2021, *57*, 673.
[42] Z. Wei, J. Hu, H. He, Y. Li, B. Xiong, *IEEE Trans. Power Electron.* 2021, *36*, 10970.
[43] A. Mallarapu, *eTransportation* 2020, *6*, 100065.
[44] T. R. Tanim, E. J. Dufek, L. K. Walker, C. D. Ho, C. E. Hendricks, J. P. Christophersen, *eTransportation* 2020, *3*, 100045.
[45] D. Sun, X. Yu, C. Wang, C. Zhang, R. Huang, Q. Zhou, T. Amietszajew, R. Bhagat, *Energy* 2021, *214*, 119025.
[46] P. Shrivastava, T. Kok Soon, M. Y. I. Bin Idris, S. Mekhilef, S. B. R. S. Adnan, *IEEE Trans. Veh. Technol.* 2021, *70*, 1200.
[47] L. Liu, J. Xu, S. Wang, F. Wu, H. Li, L. Chen, *eTransportation* 2019, *1*, 100010.
[48] Y. Zhang, R. Xiong, H. W. He, X. Qu, M. Pecht, *eTransportation* 2019, *1*, 100004.
[49] G. Sethia, S. Majhi, S. K. Nayak, S. Mitra, *IET Renewable Power Gener.* 2021, *15*, 424.
[50] M. Seo, Y. Song, J. Kim, S. W. Paek, G.-H. Kim, S. W. Kim, *Energy* 2021, *226*, 120301.
[51] Q. Zheng, Y. Yamada, R. Shang, S. Ko, Y.-Y. Lee, K. Kim, E. Nakamura, A. Yamada, *Nat. Energy* 2020, *5*, 291.

Equations:

$$\begin{cases} U_{\mathrm{L}} = U_{\mathrm{OC}} - U_{\mathrm{p}}(k) - I_{\mathrm{L}}(k)R_0 - R_{\mathrm{cd}} \\ \dfrac{\mathrm{d}U_{\mathrm{p}}(k)}{\mathrm{d}k} = \dfrac{I_{\mathrm{L}}(k)}{C_{\mathrm{p}}} - \dfrac{U_{\mathrm{p}}(k)}{C_{\mathrm{p}}R_{\mathrm{p}}} \\ U_{\mathrm{OC}} = K_1 + K_2 + \ln[S(k)] + K_3 \ln[1 - S(k)] \end{cases} \quad (1)$$

$$\frac{\mathrm{d}U_{\mathrm{p}}(k)}{d_k} = \frac{U_{\mathrm{p}}(k)T - U_{\mathrm{p}}(k-1)T}{T} = \frac{U_{\mathrm{p}}(k) - U_{\mathrm{p}}(k-1)}{T} \quad (2)$$

$$U_p(k) = \frac{C_p R_p\{U_L(k) - U_L(k-1) + (R_0 + R_{cd})[I_L(k) - I_L(k-1) + R_p I_L(k)T]\}}{T} \tag{3}$$

$$\begin{aligned} U_L(k) = {} & a_1 + a_2 U_L(k-1) + a_3 \ln[S(k)] + a_4 \ln[1 - S(k)] \\ & + a_5 I_L(k) + a_6 I_L(k-1) \end{aligned} \tag{4}$$

$$\begin{cases} a_1 = \dfrac{TK_1}{T + C_p R_p}, a_2 = \dfrac{C_p R_p}{T + C_p R_p}, a_3 = \dfrac{TK_2}{T + C_p R_p}, a_4 = \dfrac{TK_3}{T + C_p R_p} \\ a_5 = \dfrac{C_p R_p (R_0 + R_{cd}) + T(R_0 + R_p + R_{cd})}{T + C_p R_p}, a_6 = \dfrac{C_p R_p (R_0 + R_{cd})}{T + C_p R_p} \end{cases} \tag{5}$$

$$\begin{cases} K_1 = \dfrac{a_1}{1 - a_2}, \quad K_2 = \dfrac{a_3}{1 - a_2}, \quad K_3 = \dfrac{a_4}{1 - a_2} \\ R_{cd} = \dfrac{a_6}{a_2} - R_0, \quad R_p = \dfrac{a_2 a_5 + a_6}{a_2^2 - a_2}, \quad C_p = -\dfrac{a_2^2}{a_2 a_5 + a_6} \end{cases} \tag{6}$$

$$\begin{aligned} \begin{bmatrix} S_{k+1} \\ U_{1k+1} \\ U_{2k+1} \end{bmatrix} = {} & \begin{bmatrix} 1 & 0 & 0 \\ 0 & a & b \\ 0 & c & d \end{bmatrix} \begin{bmatrix} S_k \\ U_{1k} \\ U_{2k} \end{bmatrix} \\ & + \begin{bmatrix} -\eta \Delta t / C & 0 \\ e & f \\ g & d \end{bmatrix} [i_k \quad U_{OCk}] + w_k \end{aligned} \tag{7}$$

$$\begin{cases} \Phi_{k+1} = \begin{bmatrix} a & b \\ c & d \end{bmatrix}, \quad \Gamma_{k+1} = \begin{bmatrix} e & f \\ g & h \end{bmatrix} \\ U_{k+1} = -\dfrac{R_s}{R_s + R_e} U_{1k} - \dfrac{R_s}{R_s + R_e} U_{2k} - \dfrac{R_s R_e}{R_s + R_e} I_k + \dfrac{R_s}{R_s + R_e} U_{OCk} \end{cases} \tag{8}$$

$$X_k = [S_k, U_{p1,k}, U_{p2,k}]^T, \quad W_k = [W_{1,k}, W_{2,k}, W_{2,k}]^T \tag{9}$$

$$\begin{cases} X_k = f(X_{k-1}, U_k) + W_k \\ Y_k = g(X_{k-1}) + V_k \end{cases} \tag{10}$$

$$\begin{cases} \overline{x} = E(x_0), \quad P_0 = E(x_0 - \overline{x})(x_0 - \overline{x})^{\mathrm{T}} \\ y_{k|k-1}^i = g(x_{k|k-1}^i), \overline{y}_k = \sum_{i=0}^{2L} \omega_i^{\mathrm{m}} [g(x_{k|k-1}^i) + v_{k-1}^i] = \sum_{i=0}^{2L} \omega_i^{\mathrm{m}} y_{k|k-1}^i \end{cases} \tag{11}$$

$$\begin{cases} k = 0, \quad \hat{x}_0^+ = E(X_0^x), \quad R_0^+ = E(R_0) \\ P_{x0}^+ = E[(X_0^x - \hat{x}_0^+)(X_0^x - \hat{x}_0^+)^{\mathrm{T}}] \\ P_{R0}^+ = E[(R_0 - R_0^+)(R_0 - R_0^+)^{\mathrm{T}}] \end{cases} \tag{12}$$

$$X_{k|k-1} = E\{[F(X_{k-1,i}^x, I_{k-1})]|_{i=0,1,\ldots,2n}\} = \sum_{i=0}^{2n} \omega_i^{\mathrm{m}} X_{k-1,i}^x \tag{13}$$

$$x_{k-1}^i = \overline{x}_{k-1} + \left(\sqrt{(L+\lambda)P_{k-1}}\right) \tag{14}$$

$$\begin{cases} P_{y y_k} = \sum_{i=0}^{2n} w_i^{\mathrm{c}} (y_{k|k-1} - \hat{y}_k)(y_{k|k-1} - \hat{y}_k)^{\mathrm{T}} + R \\ P_{x y_k} = \sum_{i=0}^{2n} w_i^{\mathrm{c}} (y_{k|k-1} - \hat{y}_k)(y_{k|k-1} - \hat{y}_k)^{\mathrm{T}} \end{cases} \tag{15}$$

$$\begin{cases} \hat{X}_k = \hat{X}_{k|k-1} + K_k(y_k - \hat{y}_k) \\ P_{xk} = P_{xk|k-1} - K_k P_{yyk} {K_k}^T \end{cases} \tag{16}$$

$$P_c = \frac{U_c Q_c}{U_c Q_c} P_b = \lambda_b P_b \tag{17}$$

$$P'_c = \alpha P_c \tag{18}$$

$$P'_c = \alpha \frac{U_c Q_c}{U_c Q_c} P_b = 5 \times \frac{3.6 \times 2.2}{384 \times 360} \times P_b = 2.8646 \times 10^{-4} \times P_b \tag{19}$$